A higher order compact finite difference algorithm for solving the incompressible Navier–Stokes equations

Zhenfu Tian[1, *, †], Xian Liang[2] and Peixiang Yu[1]

[1]*Department of Mechanics and Engineering Science and School of Mathematical Sciences, Fudan University, Shanghai 200433, People's Republic of China*
[2]*LHD, Institute of Mechanics, Chinese Academy of Sciences, Beijing 100190, People's Republic of China*

SUMMARY

On the basis of the projection method, a higher order compact finite difference algorithm, which possesses a good spatial behavior, is developed for solving the 2D unsteady incompressible Navier–Stokes equations in primitive variable. The present method is established on a staggered grid system and is at least third-order accurate in space. A third-order accurate upwind compact difference approximation is used to discretize the non-linear convective terms, a fourth-order symmetrical compact difference approximation is used to discretize the viscous terms, and a fourth-order compact difference approximation on a cell-centered mesh is used to discretize the first derivatives in the continuity equation. The pressure Poisson equation is approximated using a fourth-order compact difference scheme constructed currently on the nine-point 2D stencil. New fourth-order compact difference schemes for explicit computing of the pressure gradient are also developed on the nine-point 2D stencil. For the assessment of the effectiveness and accuracy of the method, particularly its spatial behavior, a problem with analytical solution and another one with a steep gradient are numerically solved. Finally, steady and unsteady solutions for the lid-driven cavity flow are also used to assess the efficiency of this algorithm. Copyright © 2011 John Wiley & Sons, Ltd.

1. INTRODUCTION

The numerical solution of the unsteady incompressible Navier–Stokes (N-S) equations in primitive variable form represents a difficult computational challenge. One major problem comes from the pressure term in the momentum equations, which couples the momentum equations and must be implicitly updated for the incompressibility to be satisfied. The projection method is a widely used technique for solving viscous incompressible flow based on the primitive variable formulations. This technique introduced originally and analyzed by Chorin [1, 2] is actually a fractional step method or operator-splitting discretization scheme, in which the computations of the velocity and the pressure are decoupled through a two-step predictor–corrector procedure. In the past several decades, many improved projection methods were developed by some authors [3–9]. In the first step, an intermediate velocity field is computed by solving the momentum equations ignoring the pressure term and the incompressibility constraint. In the second step, according to Helmholtz–Hodge decomposition theorem [10], the intermediate velocity is projected to the space

---

*Correspondence to: Zhenfu Tian, Department of Mechanics and Engineering Science, Fudan University, Shanghai 200433, People's Republic of China.
†E-mail: zftian@nxu.edu.cn

of the divergence-free vector fields to get the pressure and the corrected velocity that satisfies the incompressibility condition.

For many application problems it is desirable to use higher order numerical methods to obtain accurate solution. Compact finite difference (FD) methods feature high order accuracy and smaller stencils. Recently, there has been a renewed interest in the development and application of compact FD methods for the numerical solution of the convection–diffusion and N-S equations [11–18]. It is evident that they are not only accurate and effective but also can obtain satisfactory results with a smaller grid mesh.

This paper is primarily aimed at developing a higher order compact FD algorithm, which possesses a good spatial behavior for solving 2D unsteady incompressible N-S equations in primary variable form based on the projection method. The method is constructed on a staggered grid system and has at least third-order accuracy in spatial dimension. A third-order upwind compact difference approximation proposed in [15] is used to discretize the non-linear convection terms, a fourth-order symmetrical compact difference approximation is used to discretize the viscous terms, and a fourth-order compact difference approximation on a cell-centered mesh is used to discretize the first derivatives in the continuity equation. Especially, a new fourth-order compact difference scheme for approximating the pressure Poisson equation and new explicit schemes for solving the pressure gradient are proposed on the nine-point 2D stencil. Numerical experiments are performed for the validation of accuracy and efficiency of the present algorithm.

2. MATHEMATICAL MODEL

The time-dependent incompressible N-S equations in primitive variable form can be written as

$$\mathbf{V}_t + (\mathbf{V} \cdot \nabla)\mathbf{V} + \nabla p = \frac{1}{Re}\nabla^2 \mathbf{V} \tag{1}$$

$$\nabla \cdot \mathbf{V} = 0 \tag{2}$$

where p is the pressure, $\mathbf{V} = (u, v)$ represents the velocity vector, and Re is Reynolds number.

Most numerical methods for solving Equations (1) and (2) in terms of the primitive variable use a fractional step approach. An approximation to momentum equation (1) is first made to determine a provisional velocity field, and then an elliptic equation is solved that enforces the solenoidal constraint (2) and determines the pressure.

According to Helmholtz–Hodge decomposition theorem [10], an intermediate velocity $\mathbf{V}^*$ is calculated by neglecting the contribution of the pressure gradient term. In this step, the explicit Euler scheme is used:

$$\frac{\mathbf{V}^* - \mathbf{V}^n}{\triangle t} = \frac{1}{Re}\nabla^2 \mathbf{V}^n - (\mathbf{V}^n \cdot \nabla)\mathbf{V}^n \tag{3}$$

Then, the intermediate velocity $\mathbf{V}^*$ can be decomposed into the sum of two vectors:

$$\mathbf{V}^* = \mathbf{V}^{n+1} \oplus \nabla \phi \tag{4}$$

where vector $\mathbf{V}^{n+1}$ with zero divergence denotes the velocity fields at the next time level, vector $\nabla \phi$ with zero curl. And then discretizing equation (1) and applying (3), we have

$$\frac{\mathbf{V}^{n+1} - \mathbf{V}^*}{\triangle t} = -\nabla p^{n+1} \tag{5}$$

$$\nabla \cdot \mathbf{V}^{n+1} = 0 \tag{6}$$

The pressure field p^{n+1} is obtained by taking the divergence of formula (5) and applying formula (6)

$$\nabla^2 p^{n+1} = \frac{1}{\triangle t}\nabla \cdot \mathbf{V}^* \tag{7}$$

where p denotes a pseudo-pressure when used in a semi-implicit formulation. After solving the pressure and pressure gradient, we can obtain the velocity fields at time level $n+1$ from Equation (5).

3. HIGHER ORDER COMPACT SCHEMES OF MATHEMATICAL MODEL

The staggered mesh grid point system is given in Figure 1. We approximate the problem on uniform spatial grids with step $\triangle x$ in x-direction and $\triangle y$ in y-direction. We denote by $f_{i,j}$ the approximation of a function f at the mesh points $(x_i = i\triangle x, y_j = j\triangle y)$. In addition, some difference operators used in this paper are defined as follows:

$$\delta_x^0 f_{i,j} = \frac{f_{i+\frac{1}{2},j} - f_{i-\frac{1}{2},j}}{\triangle x} \tag{8}$$

$$\delta_y^0 f_{i,j} = \frac{f_{i,j+\frac{1}{2}} - f_{i,j-\frac{1}{2}}}{\triangle y} \tag{9}$$

$$\triangle_x^0 f_{i,j} = \frac{f_{i+1,j} - f_{i-1,j}}{2\triangle x} \tag{10}$$

$$\triangle_y^0 f_{i,j} = \frac{f_{i,j+1} - f_{i,j-1}}{2\triangle y} \tag{11}$$

$$\triangle_{xx} f_{i,j} = \frac{f_{i+1,j} - 2f_{i,j} + f_{i-1,j}}{\triangle x^2} \tag{12}$$

$$\triangle_{yy} f_{i,j} = \frac{f_{i,j+1} - 2f_{i,j} + f_{i,j-1}}{\triangle y^2} \tag{13}$$

The first momentum equation is approximated at point $(i+\frac{1}{2}, j)$, the second one at the point $(i, j+\frac{1}{2})$. The continuity equation and pressure are approximated at the point (i, j).

3.1. Discretization of the intermediate velocity

The convective terms in Equation (3) are discretized by using a third-order accurate upwind compact FD approximation [15]. For example, the term $u\partial u/\partial x$ is split as follows:

$$u\frac{\partial u}{\partial x} = u^+\frac{\partial u}{\partial x} + u^-\frac{\partial u}{\partial x} \tag{14}$$
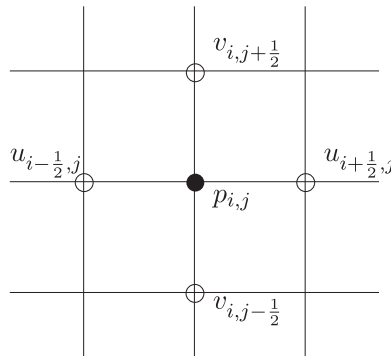

Figure 1. The staggered grid system.

where $u^{\pm} = (u \pm |u|)/2$. The terms $u^{+}\partial u/\partial x$ and $u^{-}\partial u/\partial x$ are approximated at point $(i+\frac{1}{2}, j)$ by $u^{+}_{i+\frac{1}{2},j} F^{+}_{i+\frac{1}{2},j}$ and $u^{-}_{i+\frac{1}{2},j} F^{-}_{i+\frac{1}{2},j}$, respectively. Here $F^{+}_{i+\frac{1}{2},j}$ and $F^{-}_{i+\frac{1}{2},j}$ can be approximated by the following FD schemes:

$$F^{+}_{i-\frac{1}{2},j} + 2F^{+}_{i+\frac{1}{2},j} = \frac{1}{2\triangle x}(-5u_{i-\frac{1}{2},j} + 4u_{i+\frac{1}{2},j} + u_{i+\frac{3}{2},j}) \tag{15}$$

$$2F^{-}_{i+\frac{1}{2},j} + F^{-}_{i+\frac{3}{2},j} = \frac{1}{2\triangle x}(-u_{i-\frac{1}{2},j} - 4u_{i+\frac{1}{2},j} + 5u_{i+\frac{3}{2},j}) \tag{16}$$

The viscous terms are evaluated by using a fourth-order accurate symmetrical compact FD formulation. For example, the term $\partial^{2}u/\partial x^{2}$ at point $(i+\frac{1}{2}, j)$ is approximated with $S_{i+\frac{1}{2},j}$ and

$$\frac{1}{12}S_{i-\frac{1}{2},j} + \frac{5}{6}S_{i+\frac{1}{2},j} + \frac{1}{12}S_{i+\frac{3}{2},j} = \triangle_{xx}u_{i+\frac{1}{2},j} \tag{17}$$

To obtain $S_{i+\frac{1}{2},j}$, a linear system of equation with a tri-diagonal matrix has to be solved.

In the same way, we can approximate other convection terms and viscous terms in momentum equations. After all convection and viscous terms are evaluated, we can calculate the intermediate velocity $\mathbf{V}^{*}$ through

$$(u^{*})_{i+\frac{1}{2},j} = (u^{n} + \triangle t G)_{i+\frac{1}{2},j} \tag{18}$$

$$(v^{*})_{i,j+\frac{1}{2}} = (v^{n} + \triangle t H)_{i,j+\frac{1}{2}} \tag{19}$$

where

$$G = \frac{1}{Re}(S_{i}(u) + S_{j}(u)) - u^{-}F_{i}^{-}(u) - u^{+}F_{i}^{+}(u) - v^{-}F_{j}^{-}(u) - v^{+}F_{j}^{+}(u) \tag{20}$$

$$H = \frac{1}{Re}(S_{i}(v) + S_{j}(v)) - u^{-}F_{i}^{-}(v) - u^{+}F_{i}^{+}(v) - v^{-}F_{j}^{-}(v) - v^{+}F_{j}^{+}(v) \tag{21}$$

where $u^{\pm}F_{i}^{\pm}(g)$ and $v^{\pm}F_{j}^{\pm}(g)$ are approximations of $u^{\pm}(\partial g/\partial x)_{i+\frac{1}{2},j}$ and $v^{\pm}(\partial g/\partial y)_{i,j+\frac{1}{2}}$, and $S_{i}(g)$ and $S_{j}(g)$ are approximations of $(\partial^{2}g/\partial x^{2})_{i+\frac{1}{2},j}$ and $(\partial^{2}g/\partial y^{2})_{i,j+\frac{1}{2}}$, respectively, and u, v in G, H denote the velocity at time level n.

In Equation (21), the value of velocity component v, which is defined at point $(i, j+\frac{1}{2})$, needs to be computed at the point $(i+\frac{1}{2}, j)$. In this paper, $v_{i+\frac{1}{2},j}$ is calculated by fourth-order accurate midpoint interpolation. In the same way, $u_{i,j+\frac{1}{2}}$ can be calculated.

3.2. Discretization of the pressure field and the pressure gradient

The Poisson equation for pressure can be written as

$$\nabla^{2}p = \frac{1}{\triangle t}D(\mathbf{V}^{*}) \tag{22}$$

where $D(\mathbf{V}^{*}) = (\partial u^{*}/\partial x) + (\partial v^{*}/\partial y)$, u^{*}, v^{*} are the intermediate velocities. At point (i, j), Equation (22) is discretized with a fourth-order difference approximation on the nine-point 2D stencil, which can be expressed as follows:

$$\frac{1}{12\triangle x\triangle y}\{(\lambda + \gamma)(p_{i+1,j+1} + p_{i+1,j-1} + p_{i-1,j+1} + p_{i-1,j-1} - 20p_{i,j})$$

$$+ 2(5\lambda - \gamma)(p_{i+1,j} + p_{i-1,j}) + 2(5\gamma - \lambda)(p_{i,j+1} + p_{i,j-1})\}$$

$$= \frac{1}{\triangle t}\left\{D_{i,j} + \frac{1}{12}[\triangle x^{2}(D_{xx})_{i,j} + \triangle y^{2}(D_{yy})_{i,j}]\right\} \tag{23}$$

where $\lambda = \triangle x/\triangle y$, $\gamma = \triangle y/\triangle x$, and

$$D_{i,j} = \delta_x u_{i,j}^* + \delta_y v_{i,j}^* \tag{24}$$

$$\delta_x u_{i,j}^* = \frac{1}{24\triangle x}[27(u_{i+\frac{1}{2},j}^* - u_{i-\frac{1}{2},j}^*) - (u_{i+\frac{3}{2},j}^* - u_{i-\frac{3}{2},j}^*)] \tag{25}$$

$$\delta_y v_{i,j}^* = \frac{1}{24\triangle y}[27(v_{i,j+\frac{1}{2}}^* - v_{i,j-\frac{1}{2}}^*) - (v_{i,j+\frac{3}{2}}^* - v_{i,j-\frac{3}{2}}^*)] \tag{26}$$

Equations (25) and (26) are fourth-order accurate [13]. For a fully fourth-order FD of Equation (23) we need to approximate $(D_{xx})_{i,j}$ and $(D_{yy})_{i,j}$ with second-order accuracy, which is done as follows:

$$(D_{xx})_{i,j} = \left[\left(\frac{\partial u^*}{\partial x} + \frac{\partial v^*}{\partial y} \right)_{xx} \right]_{i,j}$$

$$= \left(\frac{\partial^3 u^*}{\partial x^3} + \frac{\partial^3 v^*}{\partial x^2 \partial y} \right)_{i,j} \tag{27}$$

$$(D_{yy})_{i,j} = \left(\frac{\partial^3 u^*}{\partial x \partial y^2} + \frac{\partial^3 v^*}{\partial y^3} \right)_{i,j} \tag{28}$$

Note that

$$\left(\frac{\partial^3 u^*}{\partial x^3} \right)_{i,j} = \triangle_{xx} \delta_x^0 u_{i,j}^* + O(\triangle x^2) \tag{29}$$

$$\left(\frac{\partial^3 v^*}{\partial y^3} \right)_{i,j} = \triangle_{yy} \delta_y^0 v_{i,j}^* + O(\triangle y^2) \tag{30}$$

and

$$\left(\frac{\partial^3 v^*}{\partial x^2 \partial y} \right)_{i,j} = \frac{1}{\triangle y} \left[\left(\frac{\partial^2 v^*}{\partial x^2} \right)_{i,j+\frac{1}{2}} - \left(\frac{\partial^2 v^*}{\partial x^2} \right)_{i,j-\frac{1}{2}} \right] + O(\triangle y^2)$$

$$= \frac{1}{\triangle y}(\triangle_{xx} v_{i,j+\frac{1}{2}}^* - \triangle_{xx} v_{i,j-\frac{1}{2}}^*) + O(\triangle x^2 + \triangle y^2)$$

$$= \triangle_{xx} \delta_y^0 v_{i,j}^* + O(\triangle x^2 + \triangle y^2) \tag{31}$$

$$\left(\frac{\partial^3 u^*}{\partial x \partial y^2} \right)_{i,j} = \triangle_{yy} \delta_x^0 u_{i,j}^* + O(\triangle x^2 + \triangle y^2) \tag{32}$$

we have

$$(D_{xx})_{i,j} = \triangle_{xx}[\delta_x^0 u_{i,j}^* + \delta_y^0 v_{i,j}^*] + O(\triangle x^2 + \triangle y^2) \tag{33}$$

$$(D_{yy})_{i,j} = \triangle_{yy}[\delta_y^0 v_{i,j}^* + \delta_x^0 u_{i,j}^*] + O(\triangle x^2 + \triangle y^2) \tag{34}$$

Substituting Equations (24), (25), (26), (33), and (34) into the right-hand side of Equation (23), we obtain the following fourth-order FD scheme for the pressure Poisson equation (22) on staggered

grid system:

$$\frac{1}{12\triangle x \triangle y}[(\lambda+\gamma)(p_{i+1,j+1}+p_{i+1,j-1}+p_{i-1,j+1}+p_{i-1,j-1}-20p_{i,j})$$

$$+2(5\lambda-\gamma)(p_{i+1,j}+p_{i-1,j})+2(5\gamma-\lambda)(p_{i,j+1}+p_{i,j-1})]$$

$$=\frac{1}{12\triangle t \triangle x}\left\{\frac{1}{2}[27(u^*_{i+\frac{1}{2},j}-u^*_{i-\frac{1}{2},j})-(u^*_{i+\frac{3}{2},j}-u^*_{i-\frac{3}{2},j})]+(\triangle x)^3\triangle_{xx}[\delta^0_x u^*_{i,j}+\delta^0_y v^*_{i,j}]\right\}$$

$$+\frac{1}{12\triangle t \triangle y}\left\{\frac{1}{2}[27(v^*_{i,j+\frac{1}{2}}-v^*_{i,j-\frac{1}{2}})-(v^*_{i,j+\frac{3}{2}}-v^*_{i,j-\frac{3}{2}})]+(\triangle y)^3\triangle_{yy}[\delta^0_y v^*_{i,j}+\delta^0_x u^*_{i,j}]\right\}$$

$$\tag{35}$$

For computing velocity field, we must know the value of pressure gradient at the same grid point. As noted above, velocity components u and v are defined at points $(i+\frac{1}{2},j)$ and $(i,j+\frac{1}{2})$ on staggered mesh grid system, respectively. So the pressure gradient components $\partial p/\partial x$ and $\partial p/\partial y$ should be calculated at points $(i+\frac{1}{2},j)$ and $(i,j+\frac{1}{2})$. In the following text, we give the derivation of FD schemes to approximate the $(\partial p/\partial x)_{i+\frac{1}{2},j}$ and $(\partial p/\partial y)_{i,j+\frac{1}{2}}$. For $(\partial p/\partial x)_{i+\frac{1}{2},j}$, using Taylor expansions of $p_{i+1,j}$ and $p_{i,j}$ to point $(i+\frac{1}{2},j)$, we have

$$\left(\frac{\partial p}{\partial x}\right)_{i+\frac{1}{2},j}=\delta^0_x p_{i+\frac{1}{2},j}-\frac{\triangle x^2}{24}\left(\frac{\partial^3 p}{\partial x^3}\right)_{i+\frac{1}{2},j}+O(\triangle x^4) \tag{36}$$

Note that

$$\frac{\partial^2 p}{\partial x^2}+\frac{\partial^2 p}{\partial y^2}=\frac{1}{\triangle t}D(\mathbf{V}^*) \tag{37}$$

and

$$D(\mathbf{V}^*)=\frac{\partial u^*}{\partial x}+\frac{\partial v^*}{\partial y} \tag{38}$$

Combining Equations (37) and (38), and substituting into the second term of the right-hand side of Equation (36) and rearranging, we obtain the following fourth-order compact scheme to approximate the pressure gradient $(\partial p/\partial x)_{i+\frac{1}{2},j}$

$$\left(\frac{\partial p}{\partial x}\right)_{i+\frac{1}{2},j}=\delta^0_x p_{i+\frac{1}{2},j}+\frac{\triangle x^2}{24}\left(\frac{\partial^3 p}{\partial x\partial y^2}\right)_{i+\frac{1}{2},j}-\frac{\triangle x^2}{24\triangle t}\left(\frac{\partial^2 u^*}{\partial x^2}+\frac{\partial^2 v^*}{\partial x\partial y}\right)_{i+\frac{1}{2},j}+O(\triangle x^4)$$

$$=\delta^0_x p_{i+\frac{1}{2},j}+\frac{\triangle x^2}{24}\triangle_{yy}\delta^0_x p_{i+\frac{1}{2},j}-\frac{\triangle x^2}{24\triangle t}[\triangle_{xx}u^*_{i+\frac{1}{2},j}+\delta^0_y\delta^0_x v^*_{i+\frac{1}{2},j}]$$

$$+O(\triangle x^4+\triangle x^2\triangle y^2) \tag{39}$$

Similarly, we can obtain the fourth-order accurate compact difference approximation of $(\partial p/\partial y)_{i,j+\frac{1}{2}}$

$$\left(\frac{\partial p}{\partial y}\right)_{i,j+\frac{1}{2}}=\delta^0_y p_{i,j+\frac{1}{2}}+\frac{\triangle y^2}{24}\triangle_{xx}\delta^0_y p_{i,j+\frac{1}{2}}-\frac{\triangle y^2}{24\triangle t}[\triangle_{yy}v^*_{i,j+\frac{1}{2}}+\delta^0_x\delta^0_y u^*_{i,j+\frac{1}{2}}]$$

$$+O(\triangle x^2\triangle y^2+\triangle y^4) \tag{40}$$

3.3. Solution of Poisson equation for pressure

The solution of the pressure Poisson equation (35) will cost the maximum of the whole numerical calculating time, so people are trying to develop an efficient algorithm. In this paper we have designed a line iterative approach with an alternating direction implicit (ADI) procedure that enables us to obtain the solutions of the problems by application of the one-dimensional tridiagonal Thomas algorithm with a considerable saving in computing time.

First, rewriting the discrete pressure equation in the following:

$$2(5\lambda-\gamma)p^*_{i-1,j} - 20(\lambda+\gamma)p^*_{i,j} + 2(5\lambda-\gamma)p^*_{i+1,j} = S_{i,j}$$
$$2(5\gamma-\lambda)p_{i,j-1} - 20(\lambda+\gamma)p_{i,j} + 2(5\gamma-\lambda)p_{i,j+1} = S'_{i,j} \tag{41}$$

where

$$S_{i,j} = -(\lambda+\gamma)(p_{i+1,j+1}+p_{i+1,j-1}+p_{i-1,j+1}+p_{i-1,j-1}) - 2(5\gamma-\lambda)(p_{i,j+1}+p_{i,j-1})$$

$$+\frac{\Delta y}{\Delta t}\left\{\frac{1}{2}[27(u^*_{i+\frac{1}{2},j}-u^*_{i-\frac{1}{2},j})-(u^*_{i+\frac{3}{2},j}-u^*_{i-\frac{3}{2},j})]+(\Delta x)^3\Delta_{xx}[\delta^0_x u^*_{i,j}+\delta^0_y v^*_{i,j}]\right\}$$

$$+\frac{\Delta x}{\Delta t}\left\{\frac{1}{2}[27(v^*_{i,j+\frac{1}{2}}-v^*_{i,j-\frac{1}{2}})-(v^*_{i,j+\frac{3}{2}}-v^*_{i,j-\frac{3}{2}})]+(\Delta y)^3\Delta_{yy}[\delta^0_y v^*_{i,j}+\delta^0_x u^*_{i,j}]\right\} \tag{42}$$

$$S'_{i,j} = -(\lambda+\gamma)(p^*_{i+1,j+1}+p^*_{i+1,j-1}+p^*_{i-1,j+1}+p^*_{i-1,j-1}) - 2(5\lambda-\gamma)(p^*_{i+1,j}+p^*_{i-1,j})$$

$$+\frac{\Delta y}{\Delta t}\left\{\frac{1}{2}[27(u^*_{i+\frac{1}{2},j}-u^*_{i-\frac{1}{2},j})-(u^*_{i+\frac{3}{2},j}-u^*_{i-\frac{3}{2},j})]+(\Delta x)^3\Delta_{xx}[\delta^0_x u^*_{i,j}+\delta^0_y v^*_{i,j}]\right\}$$

$$+\frac{\Delta x}{\Delta t}\left\{\frac{1}{2}[27(v^*_{i,j+\frac{1}{2}}-v^*_{i,j-\frac{1}{2}})-(v^*_{i,j+\frac{3}{2}}-v^*_{i,j-\frac{3}{2}})]+(\Delta y)^3\Delta_{yy}[\delta^0_y v^*_{i,j}+\delta^0_x u^*_{i,j}]\right\} \tag{43}$$

The first formula of (41) is the implicit iteration of (22) in x-direction, the second one in y-direction. These two formulas should be iterated alternately in each time step. For periodical boundary problems, the main works are to solve the two linear systems with circulant coefficient matrix, which concerns about CTDMA (cyclic triple diagonal matrix algorithm). For non-periodical boundary problems, it solves mainly the two linear systems with triple diagonal coefficient matrix, which concerns about TDMA (triple diagonal matrix algorithm).

3.4. Boundary formulation for velocity and pressure

In order to match high order accuracy at boundary conditions for velocity and pressure, the high order accuracy boundary schemes are designed. Various biased FD schemes are designed for approximation to the first and second derivatives at boundary in this paper. For example, the first derivative at the boundary $j=1$ satisfies the following formulation:

$$f'_1 + \alpha f'_2 = \frac{1}{\Delta x}\sum_{i=1}^{k} a_i f_i \quad (k=1,2,\ldots,N) \tag{44}$$

The coefficients α and a_i can be determined by applying Taylor expansion and coupling to necessary of inner points scheme and accuracy. In this paper, the following biased schemes can be obtained, and some relative schemes also can be found in [19].

$$a_1 = -\frac{3+\alpha+2a_4}{2}, \quad a_2 = 2+3a_4, \quad a_3 = -\frac{1-\alpha+6a_4}{2} \tag{45}$$

where α, a_4 are free parameters, the scheme has at least second accuracy. Similarly, the following third-order and fourth-order schemes can be obtained as

$$a_1 = -\frac{11+2\alpha}{6}, \quad a_2 = \frac{6-\alpha}{2}, \quad a_3 = \frac{2\alpha-3}{2}, \quad a_4 = \frac{2-\alpha}{6} \quad \text{(third order)} \tag{46}$$

$$\alpha = 3, \quad a_1 = -\frac{17}{6}, \quad a_2 = \frac{3}{2}, \quad a_3 = \frac{3}{2}, \quad a_4 = -\frac{1}{6} \quad \text{(fourth order)} \tag{47}$$

In Equation (46), set $\alpha = 0$, the third-order explicit biased scheme is defined by

$$f_1' = \frac{1}{6\triangle x}(-11f_1 + 18f_2 - 9f_3 + 2f_4) \tag{48}$$

In Equation (45), set $\alpha = 2$, $a_4 = 0$, the third-order implicit biased scheme is defined by

$$f_1' + 2f_2' = \frac{1}{2\triangle x}(-5f_1 + 4f_2 + f_3) \tag{49}$$

With the same method, the second derivative at the boundary $j = 1$ satisfies the following formulation:

$$f_1'' + \beta f_2'' = \frac{1}{\triangle x^2} \sum_{i=1}^{k} b_i f_i \quad (k = 1, 2, \ldots, N) \tag{50}$$

From Equation (50), the following second-order and third-order biased schemes with free parameters can be defined as

$$b_1 = \beta + 2 + b_5, \quad b_2 = -(2\beta + 5 + 4b_5), \quad b_3 = \beta + 4 + 6b_5, \quad b_4 = -(1+4b_5) \tag{51}$$

$$b_1 = \frac{11\beta+35}{12}, \quad b_2 = -\frac{5\beta+26}{3}, \quad b_3 = \frac{\beta+19}{2}, \quad b_4 = \frac{\beta-14}{3}, \quad b_5 = \frac{11-\beta}{12} \tag{52}$$

Some widely used schemes are obtained from Equations (51) and (52)

$$\beta = 11, \quad b_1 = 13, \quad b_2 = -27, \quad b_3 = 15, \quad b_4 = -1, \quad b_5 = 0 \quad \text{(third order)} \tag{53}$$

$$\beta = 10, \quad b_1 = \frac{145}{12}, \quad b_2 = -\frac{76}{3}, \quad b_3 = \frac{29}{2}, \quad b_4 = -\frac{4}{3}, \quad b_5 = \frac{1}{12} \quad \text{(fourth order)} \tag{54}$$

$$\beta = 0, \quad b_1 = 2, \quad b_2 = -5, \quad b_3 = 4, \quad b_4 = -1, \quad b_5 = 0 \quad \text{(second order)} \tag{55}$$

$$\beta = 0, \quad b_1 = \frac{35}{12}, \quad b_2 = -\frac{26}{3}, \quad b_3 = \frac{19}{2}, \quad b_4 = -\frac{14}{3}, \quad b_5 = \frac{11}{12} \quad \text{(third order)} \tag{56}$$

the higher order boundary scheme can be defined by adding more stencil points in Equations (44) and (50). The schemes (49) and (53) are implicit ones that can couple to inner scheme (15), (16) to use.

Refer to Equation (44), the first derivative of pressure at boundary $i = 1$ can be written as ($\alpha = 0$)

$$\left(\frac{\partial p}{\partial x}\right)_{1,j} = \frac{1}{\triangle x} \sum_{i=1}^{k} a_i p_{i,j} (k = 1, 2, \ldots, N) \tag{57}$$

Then the boundary value of pressure at $i = 1$ can be described as

$$p_{1,j} = \frac{1}{a_1}\left[\triangle x \left(\frac{\partial p}{\partial x}\right)_{1,j} - \sum_{i=2}^{k} a_i p_{i,j}\right] \tag{58}$$

It is easy to compute $(\partial p/\partial x)_{1,j}$ by projecting momentum equation to boundary normal direction. If $k=3$ is set in Equation (58) and coupled to Equation (41), the value of inner points can be calculated by using $(\partial p/\partial x)_{1,j}$ and without considering the boundary value. After finishing, to compute the value of inner points, the boundary value can be obtained from Equation (57).

In this subsection, all the boundary schemes are designed for the left boundary; the other boundary schemes can be designed similarly.

3.5. FD algorithm

The FD algorithm based on staggered grid system is now briefly outlined.

1. The first step: compute intermediate velocity $\mathbf{V}^*$

   (a) Applying upwind compact schemes (15) and (16) to compute convective terms and symmetrical compact scheme (17) to compute viscous terms;
   (b) Applying (18) and (19) to compute intermediate velocity $\mathbf{V}^*$.

2. The second step: projection step

   (a) Applying symmetrical compact scheme (35) to compute pressure p;
   (b) Applying schemes (39), (40) to compute pressure gradient;
   (c) Applying scheme (5) to compute new velocity field at time level $n+1$.

3. Repeat process 1–2.

4. NUMERICAL EXAMPLES

In this section, we perform numerical experiments to illustrate the accuracy and effectiveness of the proposed higher order compact difference algorithm. The numerical results of three test problems are given. All results were run on a SONY PCG-V505MCP computer using double precision arithmetic.

Example 1
Consider N-S equations (1) and (2) with the initial condition [1]

$$u(x, y, 0) = -\cos(Nx)\sin(Ny)$$
$$v(x, y, 0) = \sin(Nx)\cos(Ny)$$

(59)

where $0 \leqslant x \leqslant 2\pi$, $0 \leqslant y \leqslant 2\pi$. The exact solution for this problem is given by

$$u(x, y, t) = -\cos(Nx)\sin(Ny)\exp(-2N^2t/Re)$$
$$v(x, y, t) = \sin(Nx)\cos(Ny)\exp(-2N^2t/Re)$$
$$p(x, y, t) = -\tfrac{1}{4}(\cos(2Nx)+\cos(2Ny))\exp(-4N^2t/Re)$$

(60)

where N is an integer.

The numerical solutions are obtained under uniform grids ($h = \triangle x = \triangle y$) with different mesh sizes and a fixed time step size ($\triangle t = 0.002$) and compared under the RMS (root mean square) errors of the numerical solution with respect to the exact solution. The RMS error is estimated by

$$err_{\text{RMS}} = \sqrt{\frac{1}{N_x \times N_y}\sum(\phi_{i,j\,\text{comput}} - \phi_{i,j\,\text{exact}})^2}$$

(61)

where N_x and N_y are grid points in x- and y-directions, respectively, and ϕ stands for u, v, p, and ψ.

Table I. RMS errors with the rate of convergence at $t=2$ for u, v, ψ, p ($Re=100$, $N=2$).

Grid	u-error	Rate	v-error	Rate	ψ-error	Rate	p-error	Rate
11×11	7.0070489 (−2)	—	7.0070489 (−2)	—	3.0677609 (−1)	—	1.0764149 (−1)	—
21×21	9.0692193 (−3)	3.16	9.0692193 (−3)	3.16	3.8426509 (−2)	3.21	1.0567607 (−2)	3.58
31×31	2.8851487 (−3)	2.94	2.8851487 (−3)	2.94	1.1948521 (−2)	3.00	2.9103288 (−3)	3.31
41×41	1.2238736 (−3)	3.06	1.2238736 (−3)	3.06	5.0439820 (−3)	3.08	1.1356134 (−3)	3.36
51×51	6.3063026 (−4)	3.03	6.3063026 (−4)	3.03	2.5915402 (−3)	3.05	5.3933641 (−4)	3.41

Note: $7.0070489(-2) = 7.0070489^{-2}$, etc.

Table II. Errors with the rate of convergence at $t=2$ for p and CPU times ($Re=100$, $N=2$).

Grid size	Second-order method			Present method		
	L^2-error	Rate	CPU times	L^2-error	Rate	CPU times
11×11	1.405E−01		0.281	1.076E−01		0.344
21×21	4.160E−02	1.882	0.640	1.057E−02	3.588	0.875
31×31	1.897E−02	2.016	1.984	2.910E−03	3.312	2.625
41×41	1.073E−02	2.037	5.156	1.136E−03	3.364	6.266
51×51	6.869E−03	2.044	10.141	5.393E−04	3.413	12.015
61×61	4.759E−03	2.050	19.422	2.817E−04	3.627	22.375
71×71	3.483E−03	2.056	33.265	1.554E−04	3.918	37.172
81×81	2.654E−03	2.063	55.594	8.488E−05	4.590	60.640
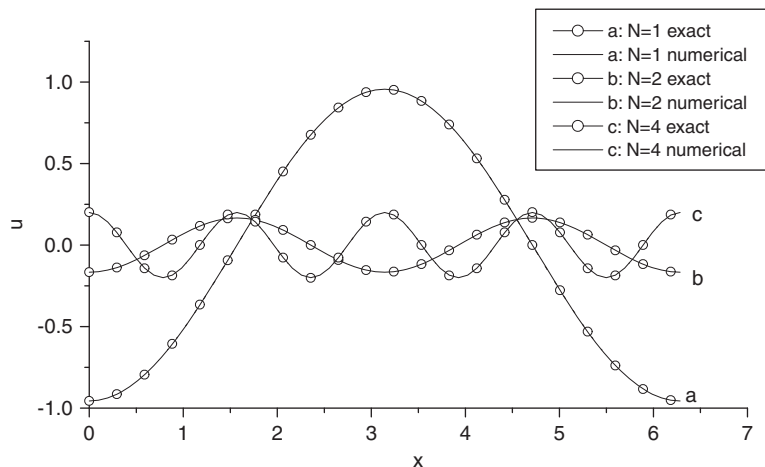
Figure 2. Velocity component u at $J=16$ for $N=1,2,4$ and $Re=100$.

The comparison of numerical results is listed in Tables I and II. The rate of convergence is estimated for velocity, vorticity, and pressure by using

$$\text{rate} = -\frac{\log(err1/err2)}{\log(N_1/N_2)} \tag{62}$$

where $err1$ and $err2$ are RMS errors with the grid system having $(N_1+1)\times(N_1+1)$ and $(N_2+1)\times(N_2+1)$ points, respectively.

It clearly shows from Table I that these values are almost 3, i.e. the present algorithm is third-order accurate in space. Table II shows the comparisons of the grid size and the CPU time required to achieve similar accuracy by both the present method and the second-order method

Table III. Grid dependence of u-velocity at the middle vertical line.

$\frac{y}{2\pi}$	33×33	65×65	97×97	129×129	161×161
$t=6$					
0.125	−1.184842	−1.179558	−1.193791	−1.195409	−1.195281
0.375	1.118550	1.174393	1.190816	1.193237	1.193570
0.625	0.721181	0.675312	0.671645	0.671016	0.670807
0.875	−0.721712	−0.675761	−0.671872	−0.671161	−0.670914
$t=8$					
0.125	−1.212727	−1.248724	−1.239336	−1.229696	−1.222598
0.375	1.205786	1.241997	1.235062	1.227654	1.222152
0.625	0.601131	0.569668	0.565301	0.564269	0.563725
0.875	−0.589285	−0.557180	−0.556850	−0.557907	−0.558628
$t=10$					
0.125	−1.114304	−1.190062	−1.218252	−1.220469	−1.218174
0.375	1.108267	1.187827	1.216600	1.219821	1.218185
0.625	0.479549	0.319745	0.312882	0.313072	0.313879
0.875	−0.511503	−0.388838	−0.372990	−0.365419	−0.360031

Table IV. Grid dependence of v-velocity at the middle horizontal line.

$\frac{x}{2\pi}$	33×33	65×65	97×97	129×129	161×161
$t=6$					
0.125	0.528987	0.573284	0.577703	0.579244	0.580072
0.375	0.286628	0.273020	0.268318	0.266371	0.265384
0.625	−0.563078	−0.588918	−0.588034	−0.586974	−0.586250
0.875	−0.248347	−0.256254	−0.257363	−0.258304	−0.258944
$t=8$					
0.125	0.626262	0.688566	0.697838	0.700261	0.701517
0.375	0.430775	0.467724	0.470392	0.470401	0.470019
0.625	−0.677859	−0.709125	−0.712632	−0.711363	−0.710431
0.875	−0.408829	−0.448764	−0.457935	−0.461006	−0.462497
$t=10$					
0.125	0.661511	0.670398	0.675042	0.679404	0.682410
0.375	0.554838	0.589328	0.580261	0.578208	0.577004
0.625	−0.633699	−0.644967	−0.649541	−0.656733	−0.662788
0.875	−0.499663	−0.558352	−0.562290	−0.564907	−0.566180

(i.e. the convective and viscous terms in the momentum equations and the pressure Poisson equation are approximated by using the standard second-order central formula). Note that the computed solutions from the present method are more accurate than that from the second-order method at the same mesh size. It is clear that the second-order method requires almost the same CPU time as does the present method for the same mesh size. It is also clear that the second-order method requires a much finer grid, hence much longer CPU time, to achieve similar accuracy as the present method. For example, in the case of 41×41 grid points, the present method requires only 6.266 s to achieve an accuracy of 1.136e−03, whereas the second-order method requires a grid of 81×81 and 55.594 s of CPU time to achieve an accuracy of 2.654e−03. The results in Table II show the superiority of the present method over the second-order method.

In Figure 2, the variation of the exact and numerical horizontal velocities u with x at $y=\pi/2$ for $N=1,2,4$ is given. One can hardly distinguish the numerical solutions from the analytical ones. This figure shows again that the present method can give the satisfying result for this problem.

Table V. Percentage difference of u-velocity at the middle vertical line with respect to the results on a gird of 161×161.

$\frac{y}{2\pi}$	33×33	65×65	97×97	129×129
$t=6$				
0.125	0.873	1.315	0.125	0.011
0.375	6.285	1.607	0.231	0.028
0.625	7.509	0.672	0.125	0.031
0.875	7.571	0.722	0.143	0.037
$t=8$				
0.125	0.807	2.137	1.369	0.581
0.375	1.339	1.624	1.056	0.450
0.625	6.635	1.054	0.280	0.097
0.875	5.488	0.259	0.318	0.129
$t=10$				
0.125	8.527	2.308	0.006	0.188
0.375	9.023	2.492	0.130	0.134
0.625	52.782	1.869	0.318	0.257
0.875	42.072	8.001	3.600	1.497

Table VI. Percentage difference of v-velocity at the middle horizontal line with respect to the results on a gird of 161×161.

$\frac{x}{2\pi}$	33×33	65×65	97×97	129×129
$t=6$				
0.125	8.807	1.170	0.408	0.143
0.375	8.005	2.877	1.105	0.372
0.625	3.952	0.455	0.304	0.124
0.875	4.092	1.039	0.611	0.247
$t=8$				
0.125	10.727	1.846	0.525	0.179
0.375	8.349	0.488	0.079	0.081
0.625	4.585	0.184	0.310	0.131
0.875	11.604	2.969	0.986	0.322
$t=10$				
0.125	3.063	1.760	1.080	0.440
0.375	3.842	2.136	0.564	0.209
0.625	4.389	2.689	1.999	0.914
0.875	11.748	1.383	0.687	0.225

Example 2

The next problem is set up to test the behavior of the discretization for non-stationary situations when steep gradients are involved. This is a doubly periodic double shear layer flow problem taken from [3], the initial conditions are taken as

$$u(x, y, 0) = \begin{cases} \tanh[(y - \pi/2)/\rho] & 0 \leqslant y \leqslant \pi \\ \tanh[(3\pi/2 - y)/\rho] & \pi \leqslant y \leqslant 2\pi \end{cases} \tag{63}$$

$$v(x, y, 0) = \sigma \sin(x)$$

where $\rho = \pi/15$ is the thickness of shear layer, $\sigma = 0.05$ is the initial perturbation which will grow with time and leads to a roll up of the shear layer. This problem, which has the characteristic of large gradient for $Re = 10000$, is an excellent case to verify the precision and stability of the numerical scheme at high wavenumbers.
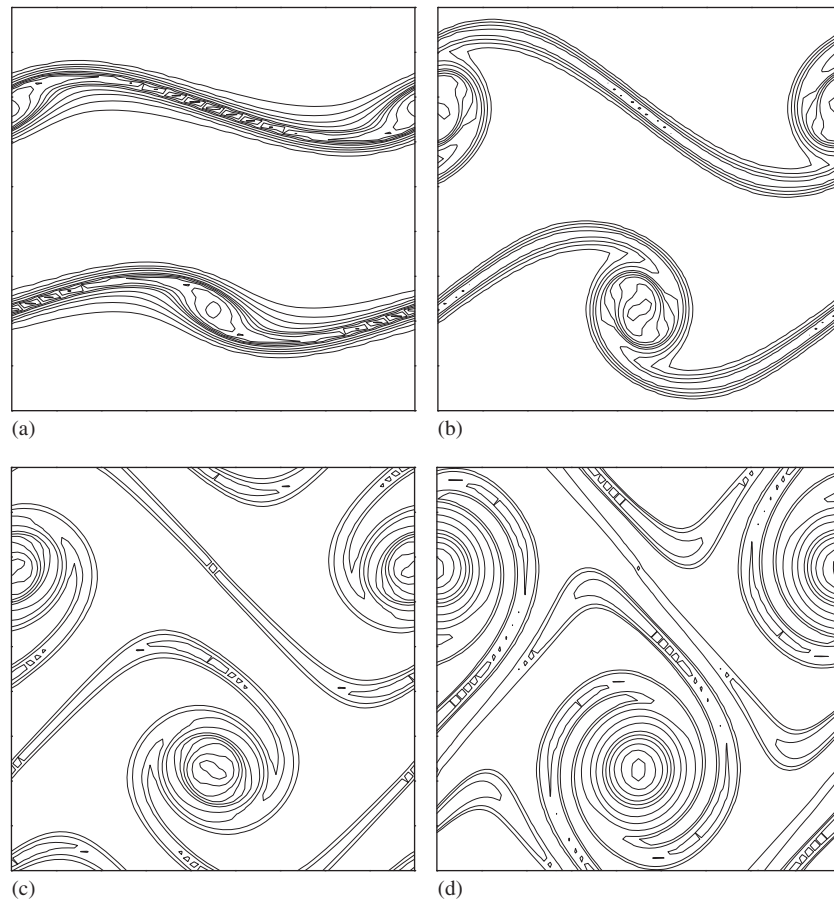
Figure 3. Vorticity contours for $\triangle x = \triangle y = 2\pi/64$: (a) $t = 4$; (b) $t = 6$; (c) $t = 8$; and (d) $t = 10$.

The incompressible N-S equations (1) and (2) with periodic boundary conditions are solved by using the present method. The calculated values of horizontal velocity u along the vertical centerline and the calculated values of vertical velocity v along the horizontal centerline at $t = 6, 8$ and 10 are listed in Tables III and IV for the grids of 33×33, 65×65, 97×97, 129×129, and 161×161. Based on the finest grid (161×161) solutions, the deviations of the results on the relatively coarser grids are shown in Tables V and VI. The solutions on a grid of 129×129 are very close to that on the finest grid, and the differences are small enough. It is believed that the grid of 129×129 points is appropriate in the present computations.

Computed vortices at different time levels for $\triangle x = \triangle y = 2\pi/64$ (i.e. 65×65 grid points) and $\triangle x = \triangle y = 2\pi/128$ (i.e. 129×129 grid points) are given in Figures 3 and 4, respectively. It is seen that very good resolution is obtained on the medium grids (e.g. 129×129 grid points). The present results are very smooth and the integration is very stable. Results from Figures 3 and 4 show that the present method is efficient for solving this problem with a steep gradient. For comparison, Figure 5 shows the flows computed at $t = 10$ by using the two second-order methods, named as the CDS1 (i.e. the spatial derivatives of velocities are approximated by the second-order difference scheme and the pressure Poisson equation is approximated by the fourth-order difference scheme) and the CDS2 (i.e. the spatial derivatives of all variables are approximated by the second-order difference scheme), respectively. Clearly, the second-order method on a grid of 161×161 has difficulty in capturing the thin shear layers, resulting in unphysical noise visible in the shear region and from the blurring effect on shear layers in the vortex core. On the contrary, the present method, even in the case of 65×65 grid points, performs very well and can capture the thin shear layers on a grid of 129×129 (see Figure 4) requiring 6787.26 s CPU time. Note also that the CDS1 method
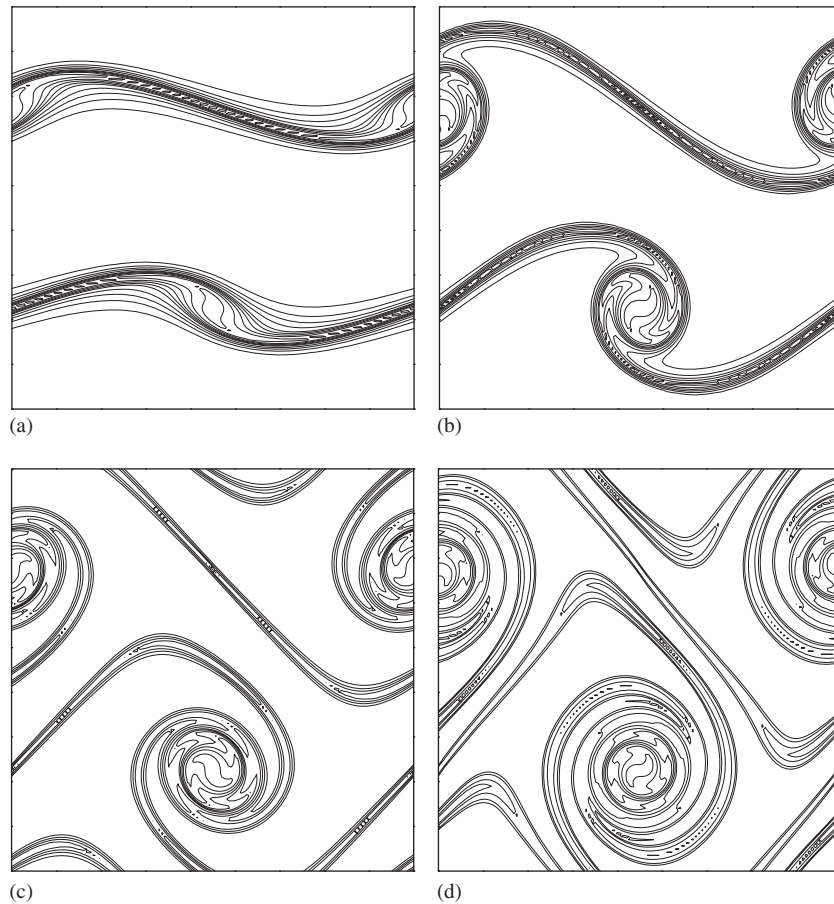
Figure 4. Vorticity contours for $\triangle x = \triangle y = 2\pi/128$: (a) $t = 4$; (b) $t = 6$; (c) $t = 8$; and (d) $t = 10$.
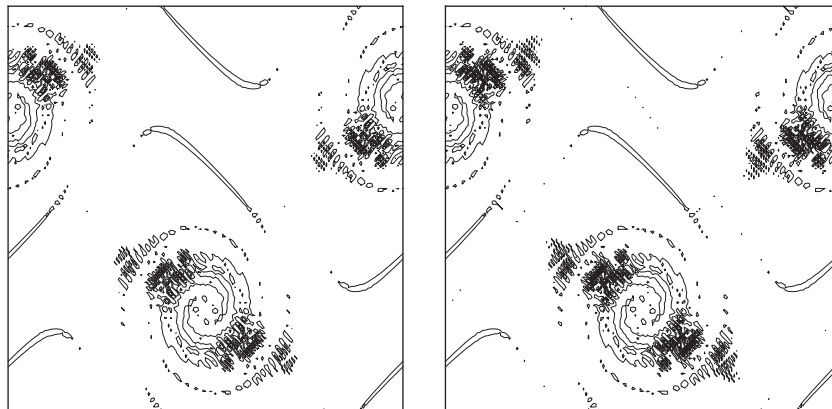

Figure 5. Vortex contours computed at $t = 10$ with (left) the second-order scheme for the velocities whereas the fourth-order scheme for the pressure and (right) the second-order scheme for all variables.

and the CDS2 method spend 14169.75 s and 12359.98 s CPU time, respectively. The numerical results from this example indicate that the present method is far superior to the second-order methods (i.e. the CDS1 and the CDS2), especially in computational accuracy, efficiency, and resolution.
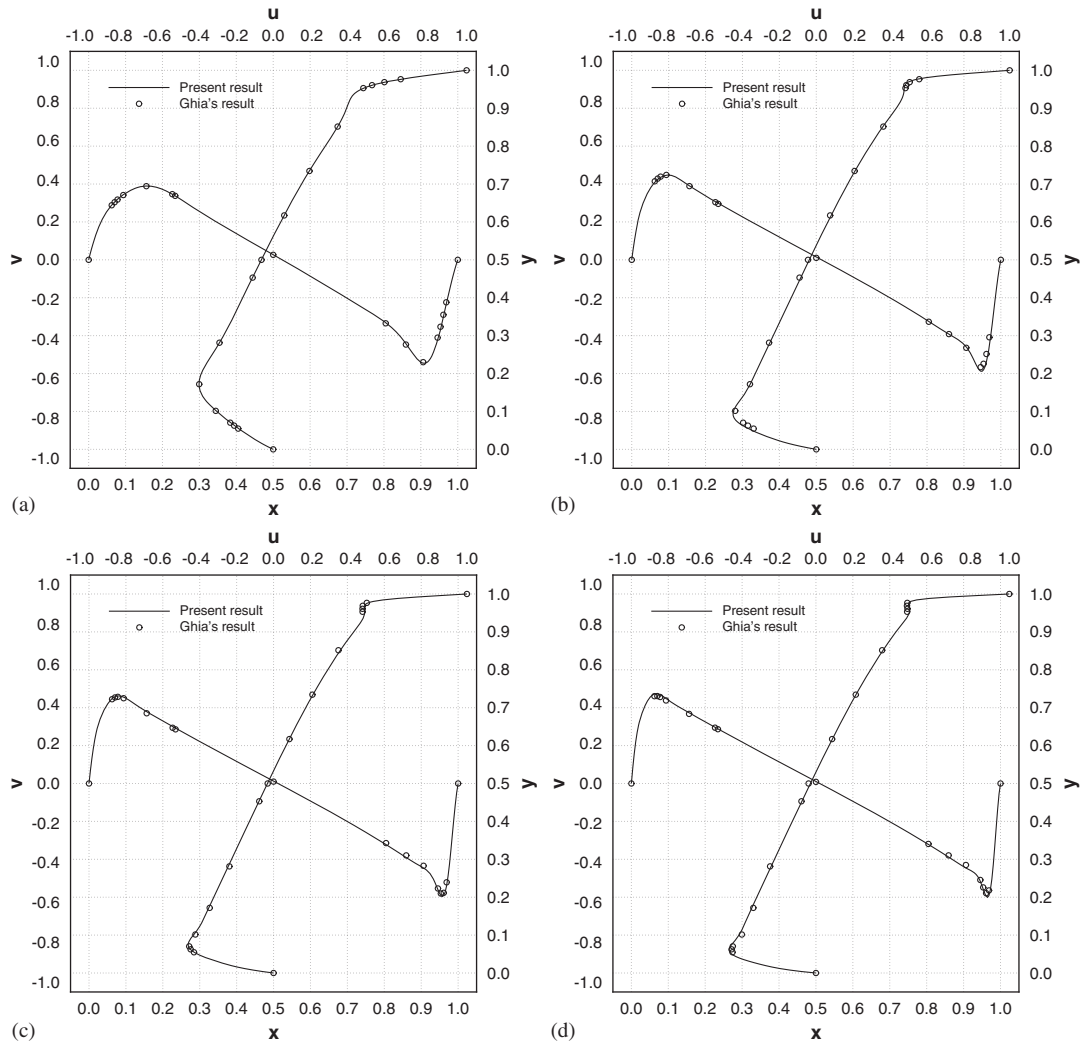
Figure 6. Profiles of u-velocity along vertical line and v-velocity along horizontal line through geometric center in cavity for (a) $Re=1000$; (b) $Re=3200$; (c) $Re=5000$; and (d) $Re=7500$.

Example 3

Finally, the two-dimensional lid-driven cavity problem is considered. Over the years, this problem is often used [6, 20–26] to demonstrate the accuracy and efficiency of numerical methods for incompressible flows. This problem is of great scientific interest because it displays almost all fluid mechanical phenomena for incompressible viscous flows in the simplest of geometric settings.

Computational region is $0\leqslant x\leqslant 1$ and $0\leqslant y\leqslant 1$, the boundary conditions are taken as

$$\begin{cases} u=1 & v=0 & y=1 \\ u=0 & v=0 & x=0, \quad 1 \text{ and } y=0 \end{cases}$$

Let

$$\triangle u_{\max}(n\triangle t)=\max[(u_{i,j}^{n+1}-u_{i,j}^{n})^2+(v_{i,j}^{n+1}-v_{i,j}^{n})^2]^{\frac{1}{2}}$$

denote the root square error at the $(n+1)$ time level. When $\triangle u_{\max}(n\triangle t)\leqslant 10^{-8}$, the solution is qualified as steady. And in each time level, to obtain the convergent solutions for the pressure,
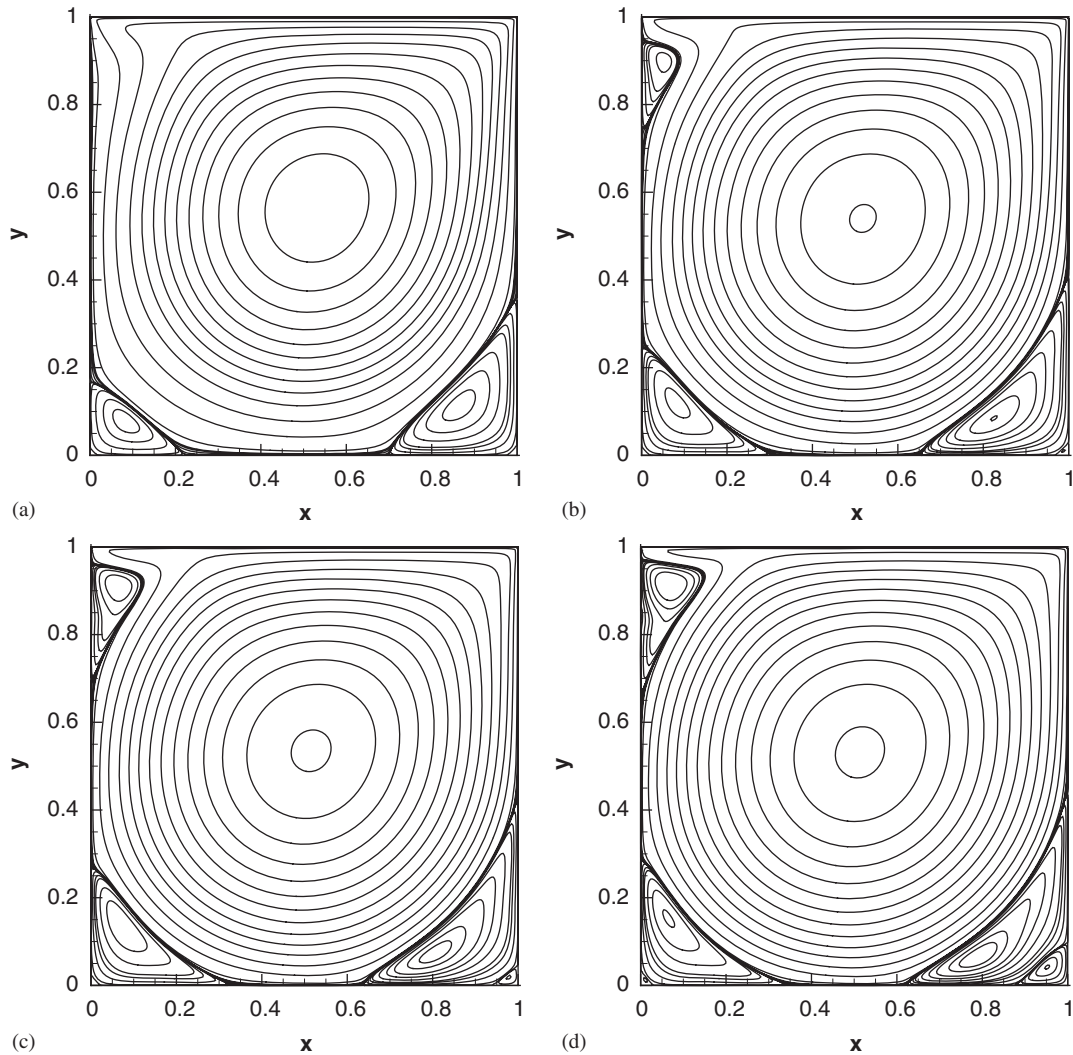
Figure 7. The steady-state streamline contours: (a) $Re = 1000$; (b) $Re = 3200$; (c) $Re = 5000$; and (d) $Re = 7500$.

more iterations are used until

$$\triangle P^m_{max} = \max | P^{m+1}_{i,j} - P^m_{i,j} | \leqslant 10^{-6}$$

where m denotes the iteration number.

Numerical solutions for the driven-cavity flow are obtained at different Reynolds numbers. In present computation, the grid mesh spacing is equal to $\frac{1}{128}$ and $\frac{1}{256}$ and the time increment is equal to 0.001.

Comparisons of some characteristic flow variables are made with previous numerical results obtained by Ghia *et al.* [25] for different values of the Reynolds number, $1000 \leqslant Re \leqslant 7500$. In Figure 6, comparisons of the vertical velocities on the horizontal centerline and the horizontal velocities on the vertical centerline of the square cavity are exhibited for $1000 \leqslant Re \leqslant 7500$ with those of Ghia *et al.* [25]. Noted that velocity profiles obtained by the proposed method on the grid mesh spacing $\frac{1}{128}$ match very well with those of Ghia *et al.* [25]. In [25], the computation is carried out on the fine grid mesh spacing $\frac{1}{256}$.
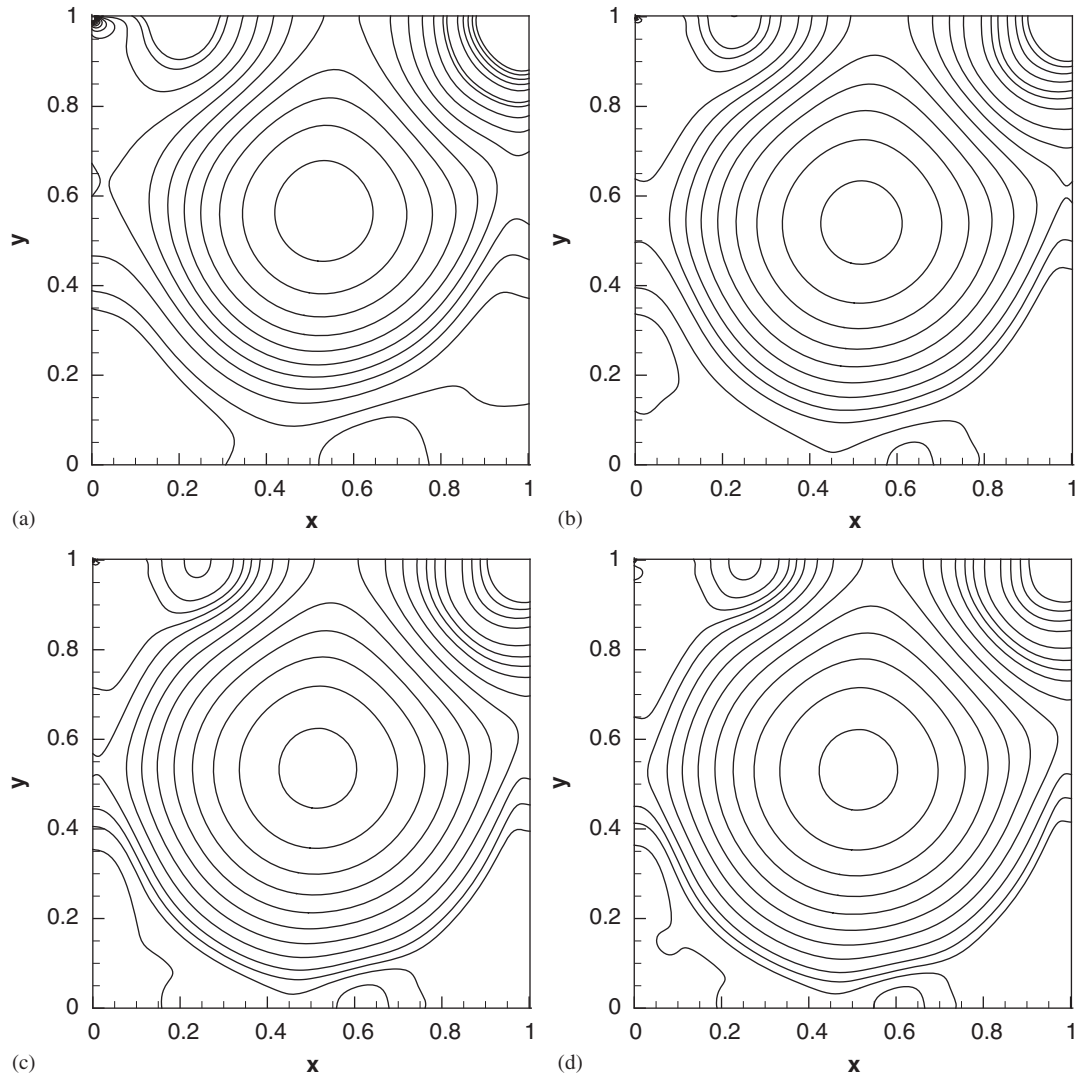
Figure 8. The steady-state pressure contours: (a) $Re=1000$; (b) $Re=3200$; (c) $Re=5000$; and (d) $Re=7500$.

Figure 7 exhibits the streamline contours for the cavity flows with Reynolds numbers 1000, 3200, 5000, and 7500. In these graphs, the typical separations and secondary vortices at the bottom corners of the cavity as well as at the top left can be seen. These stream function profiles are in very good agreement with the benchmark results of Ghia *et al.* [25] and other established results [6, 20, 21, 24] thereby confirming that the present method yields quantitatively accurate solutions. Figure 8 shows pressure contours for $1000 \leqslant Re \leqslant 7500$. Our pressure contours are compared with established results in [20]. Again, a pretty consistent comparison is obtained.

To further validate the present method quantitatively, the minimum values $u_{\min}$ and the corresponding location coordinate $y_{\min}$ of horizontal velocity along the vertical centerline, the maximum values $v_{\max}$ and the corresponding location coordinate $x_{\max}$ of vertical velocity along the horizontal centerline, and the values of streamfunction at the primary vortex center and the corresponding locations obtained numerically are collected and listed in Table VII for different Reynolds numbers ($1000 \leqslant Re \leqslant 7500$). The available comparison data from the literature are also given in this table. In Table VIII, the location of the center of secondary vortices and the value of streamfunction

Table VII. The minimum values of the velocity component u along $x=0.5$ and the corresponding y-coordinate y_{min}, the maximum values of the velocity component v along $y=0.5$ and the corresponding x-coordinate x_{max}, and the stream function ψ and the location coordinates (x, y) of the center of primary vortex for different Reynolds numbers $1000 \leqslant Re \leqslant 7500$.

Re	References	Grid size	u_{min}	y_{min}	v_{max}	x_{max}	ψ	x	y
1000	Present	129×129	−0.38134	0.1719	0.36907	0.1563	−0.116985	0.5313	0.5625
	Present	257×257	−0.38373	0.1719	0.37181	0.1602	−0.117610	0.5313	0.5625
	Ghia *et al.* [25]	129×129	−0.38289	0.1719	0.37095	0.1563	−0.117929	0.5313	0.5625
	Sahin and Owens [27]	257×257	−0.38810	0.1727	0.37691	0.1573	−0.118800	0.5335	0.5639
	Bruneau and Jouron [21]	257×257	−0.37640	0.1602	0.36650	0.1523	−0.116300	0.5313	0.5586
3200	Present	129×129	−0.42328	0.0938	0.41825	0.1016	−0.118514	0.5156	0.5391
	Present	257×257	−0.43050	0.0938	0.42703	0.0977	−0.120475	0.5195	0.5391
	Ghia *et al.* [25]	129×129	−0.41933	0.1016	0.42768	0.0938	−0.120377	0.5156	0.5469
	Sahin and Owens [27]	257×257	−0.43540	0.0921	0.43245	0.0972	−0.121628	0.5201	0.5376
5000	Present	129×129	−0.43056	0.0781	0.42814	0.0781	−0.118148	0.5156	0.5313
	Present	257×257	−0.44153	0.0742	0.44095	0.0820	−0.121062	0.5156	0.5352
	Ghia *et al.* [25]	257×257	−0.43643	0.0703	0.43648	0.0781	−0.118966	0.5117	0.5352
	Sahin and Owens [27]	257×257	−0.44731	0.0741	0.44691	0.0799	−0.122050	0.5134	0.5376
	Bruneau and Jouron [21]	257×257	−0.43590	0.0664	0.42590	0.0762	−0.114200	0.5156	0.5313
7500	Present	129×129	−0.43294	0.0625	0.43335	0.0703	−0.117218	0.5156	0.5313
	Present	257×257	−0.44873	0.0625	0.45143	0.0664	−0.121605	0.5117	0.5313
	Ghia *et al.* [25]	257×257	−0.43590	0.0625	0.44030	0.0703	−0.119976	0.5117	0.5322
	Sahin and Owens [27]	257×257	−0.45605	0.0610	0.45805	0.0670	−0.122302	0.5134	0.5289
	Bruneau and Jouron [21]	257×257	−0.43790	0.0508	0.41790	0.0625	−0.111300	0.5156	0.5234

at vortex center obtained in the present computation are compared with data from the literature [20, 21, 23, 25, 28, 29] at Reynolds numbers 1000, 3200, 5000, and 7500. It is clear from all these comparisons that the results of the present numerical method are reliable and the algorithm can be used to solve unsteady viscous incompressible flows.

A further illustration of the accuracy and the efficiency of the present method is given by computation of the unsteady flow at higher $Re = 10\,000$ on the grid mesh spacing $\frac{1}{128}$. Auteri *et al.* [30] has found that the critical Reynolds number Re_c of Hopf bifurcation from stationary state to non-stationary periodic state lies in the interval $8017.6 < Re_c < 8018.8$. Thus for the computations at $Re = 10\,000$ we expect the flow to show unsteady periodic behavior. Starting from steady-state solution obtained at $Re = 7500$, the solution reaches its asymptotic periodic state at about $t = 1240$ ($t = n \triangle t$). A series of nine instantaneous iso-streamfunction contours for one complete cycle is displayed in Figure 9. It is shown that the iso-vorticity contours are better resolved through the use of higher order compact schemes for a given fixed grid 129×129. Note that the computed solution is smooth in most of the remaining domain. The reason for this is that there are sharp gradients close to the upper moving wall. All the features shown by Fu *et al.* [15] are well represented. As observed by Fu *et al.*, persistent oscillations develop at secondary and tertiary vortices, particularly the appearance and the disappearance of the two tertiary vortices at the bottom and top lift side.

Table IX lists the comparisons of the grid size and the CPU time required to achieve accurate results (with respect to the benchmark solution [25]), at $Re = 5000$, by both the present method and the second-order method (CDS1) (i.e. the spatial derivatives of velocities are approximated by the second-order difference scheme and the pressure Poisson equation is approximated by the

Table VIII. Comparison of the results of secondary vortex at different Reynolds numbers.

Re	References	Bottom left			Bottom right		
		ψ	x	y	ψ	x	y
1000	Present[1]	2.20E−04	0.0859	0.0781	1.67E−03	0.8594	0.1094
	Present[2]	2.23E−04	0.0820	0.0781	1.69E−03	0.8672	0.1133
	Ghia *et al.* [25]	2.31E−04	0.0859	0.0781	1.75E−03	0.8594	0.1094
	Schreiber and Keller [28]	2.17E−04	0.0857	0.0714	1.70E−03	0.8643	0.1071
	Hou *et al.* [20]	2.22E−04	0.0902	0.0784	1.69E−03	0.8667	0.1137
	Bruneau and Jouron [21]	3.25E−04	0.0859	0.0820	1.91E−03	0.8711	0.1094
	Gupta and Kalita [23]	2.02E−03	0.0875	0.0750	1.70E−03	0.8625	0.1125
3200	Present[1]	1.08E−03	0.0781	0.1250	2.76E−03	0.8281	0.0859
	Present[2]	1.10E−03	0.0820	0.1172	2.79E−03	0.8281	0.0859
	Ghia *et al.* [25]	9.78E−04	0.0859	0.1094	3.14E−03	0.8125	0.0859
	Gupta and Kalita [23]	1.03E−03	0.0813	0.1188	2.86E−03	0.8125	0.0875
5000	Present[1]	1.35E−03	0.0703	0.1406	3.01E−03	0.8047	0.0703
	Present[2]	1.36E−03	0.0742	0.1367	3.04E−03	0.8086	0.0742
	Ghia *et al.* [25]	1.36E−03	0.0703	0.1367	3.08E−03	0.8056	0.0742
	Hou *et al.* [20]	1.35E−03	0.0784	0.1313	3.03E−03	0.8078	0.0745
	Bruneau and Jouron [21]	2.22E−03	0.0664	0.1484	4.65E−03	0.8301	0.0703
	Gupta and Kalita [23]	1.32E−03	0.0750	0.1313	2.96E−03	0.8000	0.0750
7500	Present[1]	1.50E−03	0.0625	0.1563	3.18E−03	0.7891	0.0625
	Present[2]	1.53E−03	0.0625	0.1563	3.22E−03	0.7930	0.0664
	Ghia *et al.* [25]	1.47E−03	0.0645	0.1504	3.28E−03	0.7813	0.0625
	Hou *et al.* [20]	1.45E−03	0.0706	0.1529	3.20E−03	0.7922	0.0667
	Bruneau and Jouron [21]	1.76E−03	0.0703	0.1289	8.32E−03	0.8828	0.0820
	Gupta and Kalita [23]	1.60E−03	0.0688	0.1500	3.05E−03	0.7813	0.0625

Notes: 1. Solved with 129×129 grid size; 2. Solved with 257×257 grid size.

fourth-order difference scheme). It is clear that the computed solutions from the present method are more close to the benchmark solution [25] than those from the second-order method at the same mesh size. Note that from Table IX, in order to obtain excellent agreement with the benchmark solutions, the present method requires a grid of 161×161 and 17798.249 s of CPU time, whereas the second-order method (CDS1) requires a grid of 257×257 and 38114.438 s of CPU time. The results in Table IX also exhibit the superiority of the present method over the second-order method.

5. CONCLUSIONS

In this work we have developed a new high order accurate compact FD projection algorithm for solving the incompressible N-S equations in primitive variables based on the staggered grid system. The present algorithm has at least third-order accuracy in spatial direction. Especially, the fourth-order compact difference scheme is proposed for approximating the pressure Poisson equation. The simple line iterative or line iterative SOR technique with an ADI procedure enables one to deal with only diagonally dominant tri-diagonal systems which can be solved by application of the one-dimensional tridiagonal Thomas algorithm with a considerable saving in computing time. This permits combining the computational efficiency of the lower order methods with superior accuracy inherent in high order approximations. The proposed discretization technique may be applicable to three-dimension case.

Numerical experiments are performed to demonstrate high accuracy and efficiency of the present method. The computational results show that, besides the excellent performances in computational
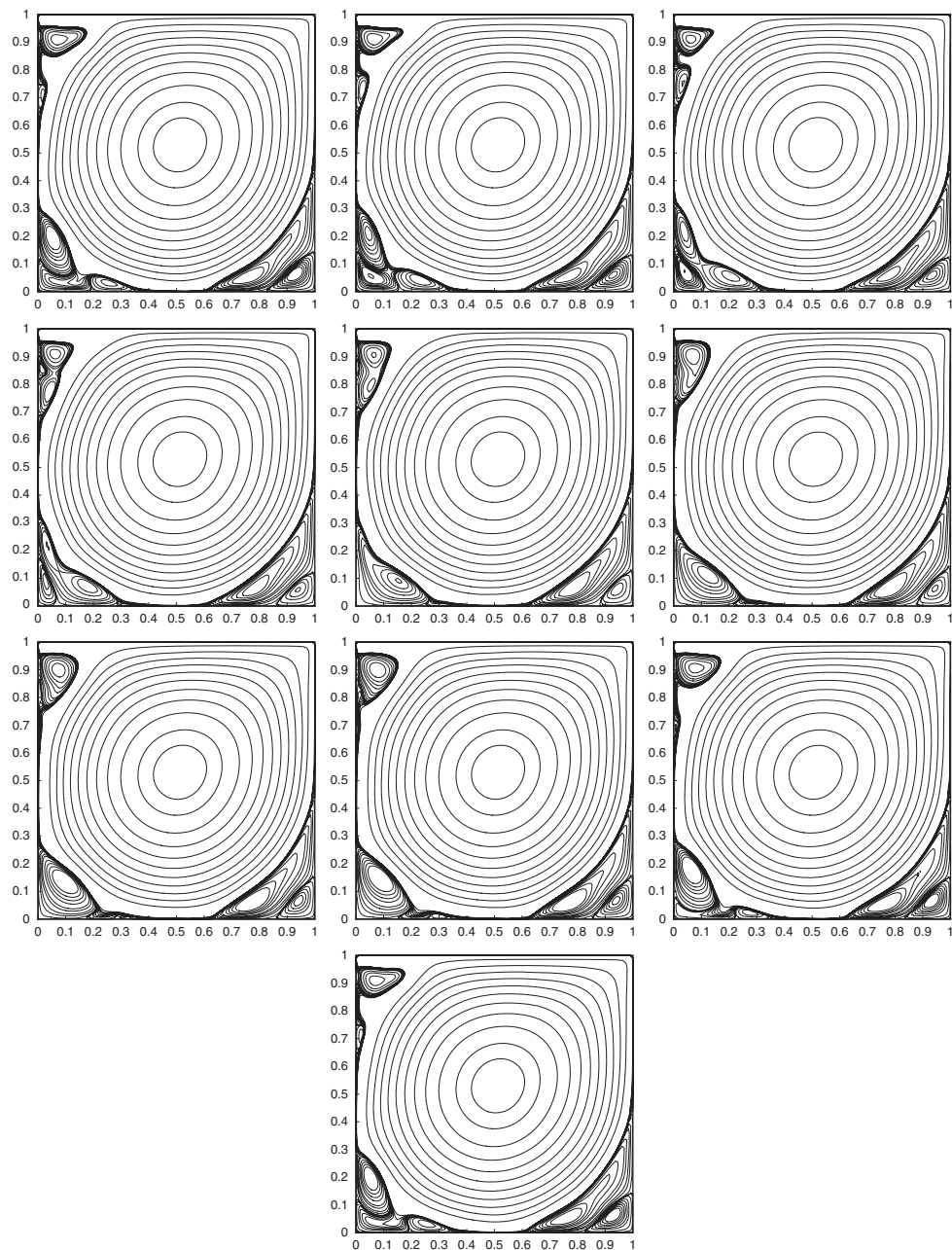
Figure 9. Continuous streamline contours for $Re = 10\,000$.

accuracy, efficiency, and stability, the method has the advantage of better scale resolution with smaller number of grid nodes. It is shown that the current method has large potential of extending to direct numerical simulation of the complex flows, including the flow problems with large gradient and high Reynolds number.

This work may be regarded as a first step towards the establishment of high order accurate and efficient algorithms for the solution of the incompressible N-S equations in primitive variables. Higher order explicit operator-splitting discretizations for temporal variables and high order compact difference schemes with high resolution for spatial variables will be the subject of forthcoming developments. In addition, we mention that the usage of non-uniform mesh becomes an

Table IX. Comparison of the velocity results of the second-order method (CDS1) with the present third-order method for lid-driven cavity flow at $Re = 5000$ and the percentage differences with respect to the benchmark solution [25].

Grid size	u_{min}	Difference (%)	v_{max}	Difference (%)	CPU time
Second-order method					
128×128	-0.40375	-7.49	0.40152	-8.01	6651.400
160×160	-0.41862	-4.08	0.41720	-4.42	9857.816
192×192	-0.42722	-2.11	0.42654	-2.28	17049.468
256×256	-0.43720	0.18	0.43665	0.04	38114.438
Third-order method					
128×128	-0.43056	-1.34	0.42184	-1.91	11844.687
160×160	-0.43619	-0.05	0.43463	-0.42	17988.249
192×192	-0.43859	0.50	0.43754	0.24	28390.206
256×256	-0.44153	1.17	0.44095	1.02	51709.853

essential aspect for dealing with irregular domain problems [31–33]. Based on the approaches proposed in [31, 32], the present scheme can be extended to the irregular case.

REFERENCES

1. Chorin AJ. Numeriacl solution of the Navier–Stokes equations. *Mathematics of Computation* 1968; **22**:745–762.
2. Chorin AJ. On the convergence of discrete approximation to the Navier–Stokes equations. *Mathematics of Computation* 1969; **23**:341–353.
3. Bell JB, Colella P. A second-order projection method for the incompressible Navier–Stokes equations. *Journal of Computational Physics* 1989; **85**:257–283.
4. E W, Liu J-G. Projection method I: convergence and numerical boundary layers. *SIAM Journal on Numerical Analysis* 1995; **33**:1017–1057.
5. E W, Liu J-G. Projection method II: Godunov–Ryabenki analysis. *SIAM Journal on Numerical Analysis* 1996; **33**:1597–1621.
6. Botella O. On the solution of the Navier–Stokes equations using Chebyshev projection schemes with third-order accuracy in time. *Computer and Fluids* 1997; **26**:107–116.
7. Brown DL, Cortez R, Minion ML. Accurate projection methods for the incompressible Navier–Stokes equations. *Journal of Computational Physics* 2001; **168**:464–499.
8. Lopez JM, Marques F, Shen J. An efficient spectral-projection method for the Navier–Stokes equations in cylindrical geometries II. Three-dimensional cases. *Journal of Computational Physics* 2002; **176**:384–401.
9. Auteri F, Parolini N. A mixed-basis spectral projection methods. *Journal of Computational Physics* 2002; **175**:1–23.
10. Ferziger JH, Peric M. *Computational Methods for Fluid Dynamics*. Springer: Berlin, 1996.
11. Li M, Tang T, Fornberg B. A compact fourth-order finite difference scheme for the incompressible Navier–Stokes equations. *International Journal for Numerical Methods in Fluids* 1995; **20**:1137–1151.
12. Li M, Tang T. A compact fourth-order finite difference scheme for unsteady viscous incompressible flows. *Journal of Scientific Computing* 2001; **16**:29–45.
13. Ma Y, Fu D, Kobarash T, Taniguchi N. Numerical solution of the incompressible Navier–Stokes equations with an upwind compact difference scheme. *International Journal for Numerical Methods in Fluids* 1999; **30**:509–521.
14. Spotz WF, Carey GF. High-order compact scheme for the steady stream-function vorticity equations. *International Journal for Numerical Methods in Engineering* 1995; **38**:3497–3512.
15. Fu D, Ma Y. High resolution scheme. In *Computational Fluid Dynamics Review*, Hafez M, Oshima K (eds). Wiley: New York, 1995; 234–250.

16. Sanyasiraju YVSS, Manjula V. Higher order semi compact scheme to solve transient incompressible Navier–Stokes equations. *Computational Mechanics* 2005; **35**:441–448.
17. Tian ZF, Ge YB. A Fourth-order compact finite difference scheme for the steady streamfunction-vorticity formulation of the Navier–Stokes/Boussinesq equations. *International Journal for Numerical Methods in Fluids* 2003; **41**:495–518.
18. Ferreira de Sousa PJSA, Pereira JCF. Fourth- and tenth-order compact finite difference solutions of perturbed circular vortex flows. *International Journal for Numerical Methods in Fluids* 2005 **49**:603–618.
19. Lele SK. Compact finite difference schemes with spectral-like resolution. *Journal of Computational Physics* 1992; **103**:16–42.
20. Hou S, Zou Q, Chen S, Doolen G, Cogley AC. Simulation of cavity flow by the Lattice Boltzmann method. *Journal of Computational Physics* 1995; **118**:329–347.
21. Bruneau CH, Jouron C. An efficient scheme for solving steady incompressible Navier–Stokes equations. *Journal of Computational Physics* 1990; **89**:389–413.
22. Ben-Artzi M, Croisille J-P, Fishelov D, Trachtenberg S. A pure-compact scheme for the streamfunction formulation of Navier–Stokes equations. *Journal of Computational Physics* 2005; **205**:640–664.
23. Gupta MM, Kalita JC. A new paradigm for solving Navier–Stokes equations: streamfunction-velocity formulation. *Journal of Computational Physicis* 2005; **207**:52–68.
24. Stéphane A, Stéphane V. A 2D compact fourth-order projection decomposition method. *Journal of Computational Physics* 2005; **206**:252–276.
25. Ghia U, Ghia KN, Shin CT. High-Re solutions for incompressible flow using the Navier–Stokes equations and a multigrid method. *Journal of Computational Physics* 1982; **48**:387–411.
26. Deng GB, Piquet J, Queutey P, Visonneau M. Incompressible-flow calculations with a consistent physical interpolations finite-volume approach. *Computers and Fluids* 1994; **23**(8):1029–1047.
27. Sahin M, Owens RG. A novel fully impicit finit volume method applied to the lid-driven cavity problem—Part I: High Reynolds number flow calculations. *International Journal for Numerical Methods in Fluids* 2003; **42**:57–77.
28. Schreiber R, Keller HB. Driven cavity flows by efficient numerical techniques. *Journal of Computational Physics* 1983; **49**:310–333.
29. Kim J, Moin P. Application of a fractional-step method to incompressible Navier–Stokes equations. *Journal of Computational Physics* 1985; **59**:308–323.
30. Auteri F, Parolini N, Quartapelle L. Numerical investigation on the stability of singular driven cavity flow. *Journal of Computational Physics* 2002; **183**:1–25.
31. Gamet L, Ducros F, Nicoud F, Poinsot T. Compact finite difference schemes on non-uniform meshes. Application to direct numerical simulations of compressible flows. *International Journal for Numerical Methods in Fluids* 1999; **29**(2):159–191.
32. Knikker R. Study of a staggered fourth-order compact scheme for unsteady incompressible viscous flows. *International Journal for Numerical Methods in Fluids* 2009; **59**:1063–1092.
33. Ben-Artzi M, Chorev I, Croisille J-P, Fishelov D. A compact difference scheme for the biharmonic equation in planar irregular domains. *SIAM Journal of Numerical Analysis* 2009; **47**:3087–3108.